

Membrane and actin reorganization in electropulse-induced cell fusion

Günther Gerisch^{1,*}, Mary Ecke¹, Ralph Neujahr^{1,‡}, Jana Prassler¹, Andreas Stengl¹, Max Hoffmann², Ulrich S. Schwarz² and Eberhard Neumann³

¹Max Planck Institute of Biochemistry, 82152 Martinsried, Germany

²Heidelberg University, Bioquant and Institute for Theoretical Physics, 69120 Heidelberg, Germany

³University of Bielefeld, Biophysical Chemistry, 33501 Bielefeld, Germany

*Author for correspondence (gerisch@biochem.mpg.de)

‡Present address: Carl Zeiss Microscopy GmbH, 81371 München, Germany

Accepted 12 February 2013

Journal of Cell Science 126, 2069–2078

© 2013. Published by The Company of Biologists Ltd

doi: 10.1242/jcs.124073

Summary

When cells of *Dictyostelium discoideum* are exposed to electric pulses they are induced to fuse, yielding motile polykaryotic cells. By combining electron microscopy and direct recording of fluorescent cells, we have studied the emergence of fusion pores in the membranes and the localization of actin to the cell cortex. In response to electric pulsing, the plasma membranes of two contiguous cells are turned into tangles of highly bent and interdigitated membranes. Live-imaging of cells double-labeled for membranes and filamentous actin revealed that actin is induced to polymerize in the fusion zone to temporarily bridge the gaps in the vesiculating membrane. The diffusion of green fluorescent protein (GFP) from one fusion partner to the other was scored using spinning disc confocal microscopy. Fusion pores that allowed intercellular exchange of GFP were formed after a delay, which lasted up to 24 seconds after exposure of the cells to the electric field. These data indicate that the membranes persist in a fusogenic state before pores of about 3 nm diameter are formed.

Key words: Actin polymerization, Cell repair, Diffusion, Electric lipid distortion, Fusion pores, Membrane fusion

Introduction

Membrane fusion in lipid vesicles and living cells can be induced by dehydration causing close apposition of the membranes (Yang and Huang, 2002; Kozlovsky et al., 2004), by proteins that reduce the energy for membrane curvature and hydrophobic interaction (Chernomordik and Kozlov, 2008; Kozlov et al., 2010; Qian and Huang, 2012), or by electric pulses, which temporarily distort the lamellar arrangement of lipids (Neumann et al., 1989). Initial studies showed that electric pulsing is an efficient method of fusing plant protoplasts (Senda et al., 1979), *Dictyostelium* cells (Neumann et al., 1980) and various mammalian cells (Zimmermann and Vienken, 1982). This method has been applied to produce hybridomas for monoclonal antibody production (Lo et al., 1984) and to generate hybrids of malignant tumor cells with dendritic cells for their use as a cancer vaccine (Kjaergaard et al., 2003).

In general, the fusion of two lipid membranes is initiated by local hydrophobic contact between two merging bilayers (Qian and Huang, 2012). During this state, splayed lipids are proposed to bridge with their hydrophobic tails the apposed leaflets of the two bilayers (Smirnova et al., 2010). This transition state is followed by a metastable intermediate called the stalk state (Yang and Huang, 2002; Kozlovsky et al., 2004; Markin et al., 1984; Markin and Albanesi, 2002; Shillcock and Lipowsky, 2005). In this state the two contacting leaflets of the lipid bilayer membranes merge, resulting in a hemifusion diaphragm that separates the two aqueous compartments. Only after the formation of pores in this bilayer, the boundary separating the

compartments will become permeable for aqueous solutes such as the GFP used in the present paper.

As revealed by molecular dynamics simulations (Smirnova et al., 2010; Shillcock and Lipowsky, 2005) and by imaging the electric-pulse induced fusion of phosphatidylcholine vesicles with a temporal resolution of 50 μ seconds (Haluska et al., 2006), the fusion of closely apposed lipid membranes is a fast process proceeding in the micro- to millisecond range. In SNARE-mediated membrane fusion experiments, the delay between docking of a vesicle to a planar membrane and its fusion was about 120 milliseconds (Kiessling et al., 2010). In contrast, membrane fusion in erythrocyte ghosts can be delayed for several seconds or minutes after electric pulsing (Dimitrov and Sowers, 1990). This means, the electric pulses initiate a sequence of processes that, after termination of the electric field, continue to produce a long-lived fusogenic state that precedes mixing of the membranes (Sowers, 1986).

In comparison to the fusion of lipid vesicles, the fusion of living cells is complicated by the presence of an actin network that is anchored to the membrane. The actin cytoskeleton may influence fusion by virtue of its membrane bending activity, and it may positively or negatively influence membrane resealing after electroporation (Teissie and Rols, 1994). Early work on mammalian cells showed that microtubules disassemble concomitantly with cell fusion, but these studies revealed no gross changes in the organization of actin (Blangero et al., 1989).

Electric pulsing is an established technique of fusing the membranes of lipid vesicles and of fusing entire cells to produce

giant multinucleate cells with no need for any chemical treatment. The electric pulses are short-lived, and the sequence of alterations in the plasma membrane initiated by them proceed after cessation of the stimulus autonomously up to complete membrane fusion. Because of the high conductivity of the cytoplasm relative to the plasma membrane, the strength of the electric field peaks at the cell surface, thus minimizing damage to the interior of the cell. To explore the generation of membrane curvature and the role of the actin cytoskeleton in electric-pulse induced cell fusion, we have combined electron microscopy of early fusion stages with quantitative fluorescence microscopy. Electron microscopy revealed clusters of highly bent membranes in the area of fusion. The formation of pores was monitored during the fusion of GFP-expressing with non-expressing cells. Live-cell imaging of filamentous actin revealed the accumulation of actin at the site of fusion, bridging the gaps in the fragmenting membranes and retarding complete fusion.

Results

Shape and performance of electrofused cells

When starved cells of *D. discoideum* develop, they become elongated and acquire adhesiveness to assemble into streams directed toward aggregation centers (compare Fig. 1A with Fig. 1E). To see whether electrofused cells maintain their developmental capacities, we have fused cells either at the beginning of starvation (Fig. 1B–D) or after development to the aggregation-competent stage (Fig. 1F–H). The undeveloped cells displayed smooth portions of their surface as well as portions covered with protrusions such as filopodia (Fig. 1B). Some of the cells formed multiple fronts (Fig. 1C) and broad, sub-divided leading edges (Fig. 1C, top of the cell). Individual fronts exerted protrusive activities on the glass surface, resulting in traction-mediated fission of the cell (Fig. 1D).

At the aggregation-competent stage, giant cells cohered with smaller ones, forming aggregates of cells with extremely heterogeneous sizes (Fig. 1F). Adhesion between giant cells was strong enough for pulling out long extensions that connected them (Fig. 1G). Compact clusters of giant and smaller cells resembled aggregation centers (Fig. 1H). These data indicate that

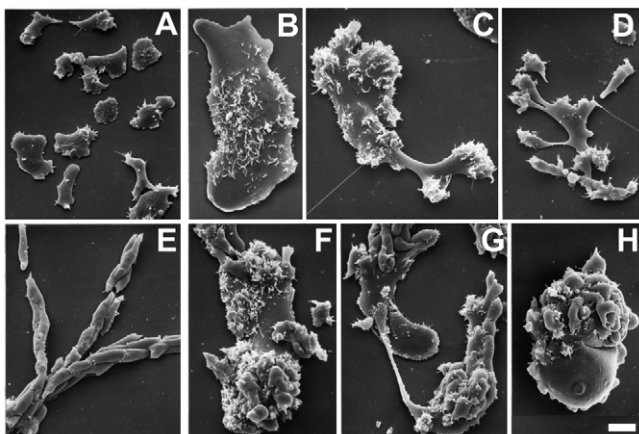


Fig. 1. Shape, size and behavior of electrofused cells in comparison to control cells. (A–D) Cells of *Dictyostelium discoideum* before (A) and after (B–D) fusion, shortly after the end of growth. (E–H) Developed, unfused (E) and fused (F–H) cells that are aggregating. The scanning electron micrographs display cells migrating on a glass surface. Scale bar: 10 μm .

the giant cells produced by electric fusion keep the characteristics of their developmental stage.

GFP transfer through fusion pores as a function of time

To record the time course of fusion, GFP-expressing cells were mixed with unlabeled or differently labeled cells. Flow of GFP from the donor to the acceptor cell was determined by scoring fluorescence intensities at intervals of about 0.5 seconds in one confocal plane through the pair of cells. In the example shown in Fig. 2A, the GFP-expressing donor cell (green) is displayed on the left and the acceptor cell on the right. The acceptor cell is labeled with mRFP-LimE Δ for filamentous actin (red). This actin label marks the fusion zone while the GFP diffuses from the donor into the acceptor cell. The diffusion of GFP is shown, separate from the actin label in supplementary material Movie 1. A non-fusing cell on top of the fusing pair serves as a reference. In this particular case the transport of GFP through the fusing membranes became detectable at 6 seconds after electric pulsing.

In order to determine concentrations c we scanned fluorescence intensities I , i.e. quantities of n GFP molecules in arbitrary units per volume element (voxel). We have normalized I to the highest value in our data set, such that all values are between 0 and 1. The mean fluorescence intensity \bar{I} within the confocal plane of each cell was taken as an estimate of the mean GFP concentration \bar{c} in the respective cell. Fig. 2B shows the decrease of $\bar{I}(t)$ in the donor cell and its increase in the acceptor cell as a function of time t after electric pulsing.

Release of GFP into the extracellular space as a result of electroporation was estimated by calculating the average of total fluorescence intensities in the donor and acceptor cell. These average intensities slowly declined, beginning with electric pulsing (Fig. 2C).

The rate of the GFP flow can be calculated from the decrease of $\bar{I}(t)$ in the donor cell and also, with opposite sign, from its increase in the acceptor cell. To plot the rate of outflow from the donor and the rate of inflow into the acceptor cell in terms of comparable quantities of GFP molecules, the mean concentration \bar{c} was multiplied with the volume of the corresponding cell. Estimates of the volumes of donor and acceptor cell were obtained by z-scanning through the entire pair of cells at the end of fusion. The rates of flow are then the time derivatives of GFP quantities that leave the donor or enter the acceptor cell (Fig. 2D). To minimize the influence of leakiness, we calculated the average changes of fluorescence intensities in the donor and acceptor cell (Fig. 2E).

In Fig. 3A the spatial profiles of the fluorescence intensities $I(x)$ are shown, where $I(x)$ reflects the GFP concentrations $c(x)$ along the scan displayed in the first frame of Fig. 2A. The curves of $I(x)$ refer to various times from the beginning of fusion to almost complete equilibration in the two cells. At the cell–cell boundary, the profiles of $I(x)$ reveal a quasi-linear section, from which the steepest portion of the gradient $\Delta I(x)/\Delta x$ for each time point can be obtained (Fig. 3B). The temporal evolution of the fluorescence profiles is displayed in the right panel of supplementary material Movie 1. The slope of the gradients plotted in Fig. 3C proved to be a sensitive indicator of the diffusion of GFP from one cell to the other. These data indicate that it took 8 seconds from the onset of GFP exchange up to decline of the slope of the gradient down to $-0.1 \Delta I/\mu\text{m}$ at the cell–cell boundary, i.e. to almost complete equilibration of GFP between the fusing cells (Fig. 3C).

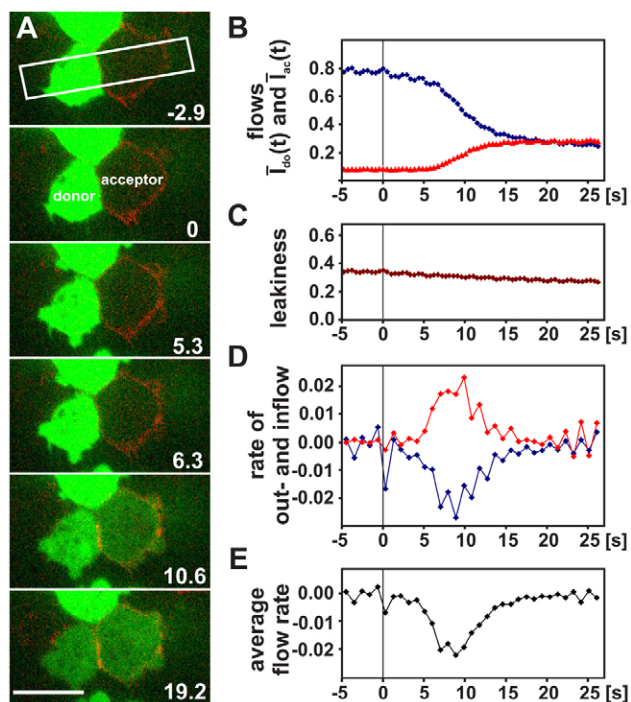


Fig. 2. GFP transfer in fusing cells. (A) Two fusing cells, one labeled with free GFP in the cytoplasm, and the other with mRFP-LimE Δ , a probe for filamentous actin. Fusion of the same cells is shown in supplementary material Movie 1. Zero time refers to the end of electric pulsing. The time series of merged images shows GFP fluorescence in green and the actin probe in red. Scale bar: 10 μm . Box in the top panel indicates the position of the line scans shown in Fig. 3A. (B) Mean fluorescence intensities in the plane of focus of the donor (\bar{I}_{do}) and acceptor (\bar{I}_{ac}) cell shown in A. The decline of \bar{I}_{do} (blue curve) and the increase of \bar{I}_{ac} (red curve) are displayed as a function of time after the end of pulsing ($t=0$). After fusion is completed, the intensity in both cells is below half of the initial intensity in the donor cell, consistent with the 1.7-fold larger volume of the acceptor cell. Estimates of volumes were $v_{do}=374 \mu\text{m}^3$ for the donor cell and $v_{ac}=638 \mu\text{m}^3$ for the acceptor cell. (C), total fluorescence intensities in the donor plus acceptor cell as a measure of leakiness. The loss of GFP from the cells through electroporation was calculated from $\frac{\bar{I}_{do} \times v_{do} + \bar{I}_{ac} \times v_{ac}}{V}$. \bar{I}_{do} and \bar{I}_{ac} are the mean fluorescence intensities in the donor and acceptor cell; V is the sum of the volumes. (D), rates of GFP flow calculated from \bar{I} scaled to volume. The flow rates are defined as $\frac{\Delta \bar{I}(do,ac)}{s} \times \frac{v(do,ac)}{V}$. The rates of outflow from the donor cell (blue) and of inflow into the acceptor cell (red) are plotted separately. To reduce fluctuations, data acquired at about 0.5-second intervals were averaged pairwise, such that the temporal resolution is now 1 second. (E) Mean rates of the in- and outflow of GFP shown in D, plotted as flow rate from the donor to the acceptor cell. In this pair of cells, the maximal rate was reached at 9 seconds after pulsing.

Simulation of GFP diffusion during fusion pore opening

In an attempt to deduce the kinetics of fusion pore opening from the experimental data, we employed computer simulation with the Smoldyn program (Andrews et al., 2010). Smoldyn is a particle-based stochastic simulation tool for reaction-diffusion systems in user-defined geometries. This tool has recently been used to simulate sequestration of CaMKII in neural dendritic spines (Khan et al., 2012) and to investigate diffusion constraints in the nuclear membrane of budding yeast during cell division (Boettcher et al., 2012).

In our simulations we modeled the donor and acceptor cells as rectangular boxes with a length of 8 and 9 μm , respectively, in agreement with the approximate cell lengths in the experiment shown in Fig. 2A. The other two dimensions have been chosen such that the volumes of the two boxes correspond to the experimentally determined cell volumes $V_{\text{donor}}=374 \mu\text{m}^3$ and $V_{\text{acceptor}}=638 \mu\text{m}^3$. Assuming, for reasons of simplicity, a single fusion pore, we simulated four different dependencies of the pore radius r on the time t : $r \sim t^{1/2}$, $r \sim t$, $r \sim t^2$, and $r \sim t^4$. Three screenshots of the simulation assuming $r \sim t$ are shown in Fig. 4A.

In Fig. 4B we show the mean flow rates for the four simulations. The onset of noticeable flows and the shape of the graphs differ between the different simulations. Noticeable flow occurs first for the $r \sim t^{1/2}$ dependency as there is a large initial change in the pore radius, in contrast to the $r \sim t^4$ dependency where noticeable flow occurs only very late, because in the initial phase of pore opening the radius increases slowly. In general, the difference between the opening dynamics is remarkably small. In Fig. 4C we fit the data of simulation to the experimental results. The linear and the quadratic opening dynamics fit the experimental data best, however, also the graphs for the other two opening scenarios are not too far off. This reflects the general challenge that diffusion leads to broad distributions in space and time, thus making it difficult to estimate the exact dynamics. These results are not dependent on whether cubic or spherical cells are used in our simulations.

In Fig. 4D we show simulations of the spatial distributions of GFP in the donor and acceptor cell for $r \sim t$ at different times of pore opening. Near the boundary between the donor and acceptor cell, gradients as in the experimental data can be identified. However, the simulated gradients are much steeper at the contact zone due to the assumption of a perfectly planar and vertical membrane between the donor and acceptor cell.

Variability of delay times and asynchronous multiple fusions

Fig. 2 shows that cell fusion induced by electric pulses can be divided into two phases: (1) a delay between the end of exposure to the electric field and the beginning of GFP diffusion from one cell to the other, (2) the opening and widening of pores that allow GFP to permeate, up to complete dispersal of the membranes that had separated the cells. The duration of the first phase proved to be highly variable. Table 1 provides an overview of delay times, which varied from less than 1 second to 25 seconds. These data indicate that the primary changes in the membranes of electrically stimulated cells can rest for half a minute before pores start to form that allow GFP to pass. The opening period of pores from the first detectability of GFP flow to its maximal rate varied in six fusions with an average and standard deviation of 4.7 ± 2.2 seconds.

Intermediate stages of membrane fusion

In sections of cells fixed within 3 minutes after electric pulsing, abundant plasma membrane fusion is evident. Fig. 5A shows continuity of the cytoplasm in a syncytium displaying nine nuclei in the plane of the section. At this stage, cytoplasmic bridges are of variable sizes, and the fused portions of the syncytium are not yet condensed into a compact cell body.

Characteristic of fusing cells are multiple complexes of interdigitated membranes with small radii of curvature (Fig. 5B). The radii of positive curvature vary in the electron microscopic images between 13 and 105 nm, half of them (11 out of 22 radii measured) are small between 13 and 33 nm. The radii

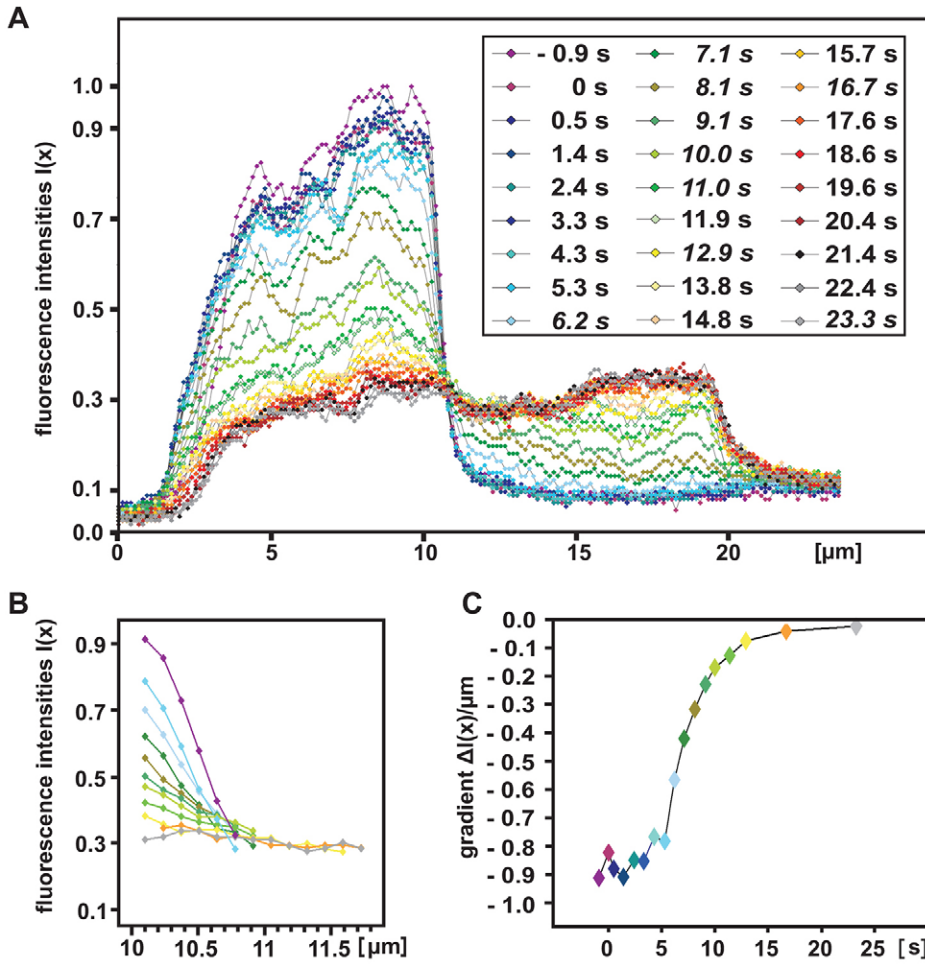


Fig. 3. Spatial profiles of fluorescence intensities $I(x)$ along the scan displayed in the first frame of Fig. 2A. (A) Profiles representing the spatial distributions $I(x)$ normal to the plane of fusion. Time of the scans is color-coded as shown in the inset. Italicized numbers in the inset refer to the sections of the profiles shown in detail in B. (B) Profiles of fluorescence intensities around the boundary of the fusing cells; time is color-coded as in A. The first curve represents the apparent slope before permeabilization of the membranes. This slope reflects the limit of optical resolution, to which deviation of the membranes from verticality and planarity may contribute. Single scans are shown in the right panel of supplementary material Movie 1. (C) Apparent gradients near the boundary between the fusing cells, determined from the profiles of fluorescence intensities in B. Slope of the gradients is presented as a function of time. Zero time refers to the end of electric pulsing.

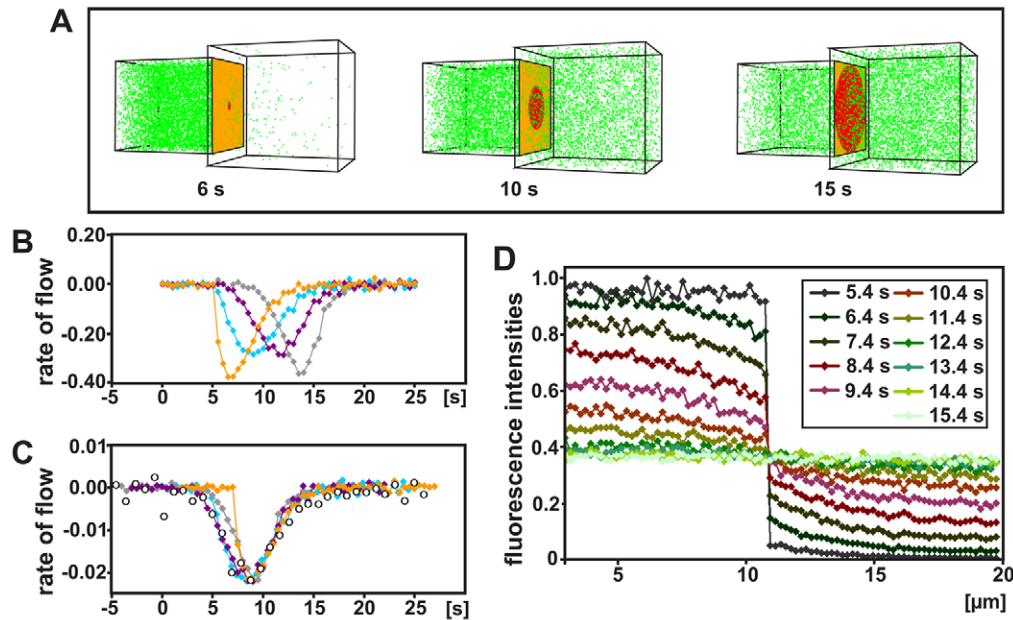


Fig. 4. Simulated rates of flow and spatial profiles of GFP molecules during the opening of a fusion pore. (A) Illustration of the GFP distributions (green) in the donor (left) and acceptor (right) cells. The size of the fusion pore (red) is displayed at three points of time after electric pulsing, assuming $r \sim t$ and a delay of 5 seconds before the onset of pore opening. (B) Rates of flow of GFP out of the donor cell calculated on the basis of $r \sim t^{1/2}$ (orange), $r \sim t$ (blue), $r \sim t^2$ (purple) or $r \sim t^4$ (grey). In all four simulations, pore opening is assumed to start at 5 seconds. (C) Fit of the simulations shown in B to the experimental data (white circles). The four simulations are individually shifted along the time axis, and the maxima are normalized to the experimental rate of flow. Both modifications are allowed because the beginning of pore opening is not defined in the experiments and the amplitudes of the simulated flow rates depend on the chosen number of particles. (D) Spatial distributions simulated for $r \sim t$. Time after the end of pulsing is color-coded as indicated in the inset. The data are aligned with the experimental results along the x -axis using the border between the two cells as a reference position.

Table 1. Delay between the end of pulsing and the beginning of visible diffusion into the acceptor cell

| Number of fusion event | Delay [s] |
|------------------------|-----------|
| 1 | 0.1 |
| 2 | 1.3 |
| 3 | 23.6 |
| 4 | 11.2 |
| 5 | 13.8 |
| 6 | 4.2 |
| 7 | 25.2 |
| 8 | 15.2 |
| 9 | 6.5 |

of negative curvature vary between 21 and 95 nm, the smaller ones (9 of 17) between 21 and 41 nm. These complexes of membranes surround halos of cytoplasm that is free of organelles and depleted of ribosomes (Fig. 5C,D), as it is typical of the actin-rich cell cortex (Medalia et al., 2002). It appears, therefore, that portions of the fusing plasma membranes bend and eventually vesiculate, underlaid by an actin sheet derived from the disrupted cell cortex. In the following, we will localize actin-coated, vesiculating membranes to the fusion zone.

Reorganization of the actin cortex during cell fusion

To explore the fate of the actin cortex during and after membrane rupture in live cells, we double-labeled cells with the membrane-integrating styryl dye FM4-64 and with LimEΔ-GFP as a label for filamentous actin. The cells were transferred to a microchamber that allows imaging of individual cells before and during the fusion. An overview on multiple fusions is provided in supplementary material Movie 2.

Fig. 6 shows a pair (Fig. 6A–D) and a group of four (Fig. 6E–H) fusing cells. Fig. 6A,E displays in merged images the membrane (red) and the actin (green) labels; Fig. 6B,F shows the membrane label; and Fig. 6C,G the actin label separately. The merged images show in the fusion zones a conversion from predominantly red into green fluorescence. The separate labels indicate that this change is due to a decline of the membrane label as well as an increase in the actin label. In Fig. 6D,H the changes of the actin profile in relation to membrane disruption are quantified (see also supplementary material Movies 3, 4). In cross-sections through an incipient membrane gap, cortical actin (green) increased within an interval of 4 to 6 seconds to a peak while the membrane label (red) declined. These data demonstrate that actin accumulates in the zone of cell fusion, bridging the gap between the disrupted membranes.

To explore the influence of filamentous actin on fusion of the cells, we treated cells prior to electric pulsing with 5 or 10 μM latrunculin A. A concentration of 5 μM has been shown to inhibit the polymerization of actin efficiently (although not completely) (Gerisch et al., 2004). The rounded cells still fused after a delay. However, their fusion was distinguished from that of untreated cells by rapid rupture of the membranes in the fusion zone (see supplementary material Movie 5). Delays in the onset of cell fusion were not dependent on an intact actin network. In the presence of 5 μM latrunculin A, the delays between the end of electric pulsing and the beginning of visible membrane rupture were 29 ± 14 (s.d. of 7 fusion events, a late fusion after 146 seconds not considered) and at 10 μM the delays were 20 ± 1 (s.d. of 5 events).

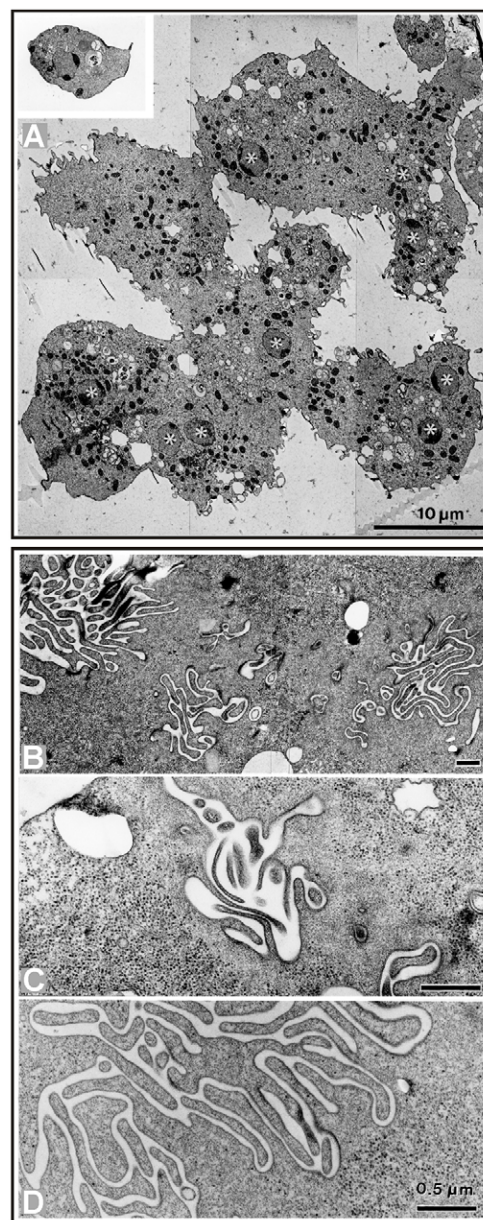


Fig. 5. Transmission electron micrographs of fusing cells. (A) Syncytium generated by electric fusion, consisting of cells connected by cytoplasmic bridges, in comparison to an unfused mononucleate cell (inset on top). The syncytium displays nine nuclei (asterisks) in the plane of the section. (B–D) Complex patterns of interdigitated membranes in areas of cell fusion. An overview of complexes in the fusion zone is shown in B. These membrane complexes are embedded into cytoplasmic areas that are free of organelles and depleted of ribosomes, which are recognizable outside these areas as dark dots in C,D. Scale bars: 10 μm (A); 0.5 μm (B–D).

Fate of the vesiculated plasma membrane

Residual membrane vesicles are displaced from the zone of cell fusion in the form of protrusions pointing into the cytoplasm. In supplementary material Movie 2, the arrow points to a vesicle that moves out of the zone in a straight line with an average velocity of 0.5 μm/second. No actin is seen to be associated with the moving vesicle, suggesting that the movement is microtubule-based. In fact, dynein has been shown to be associated with the plasma membrane

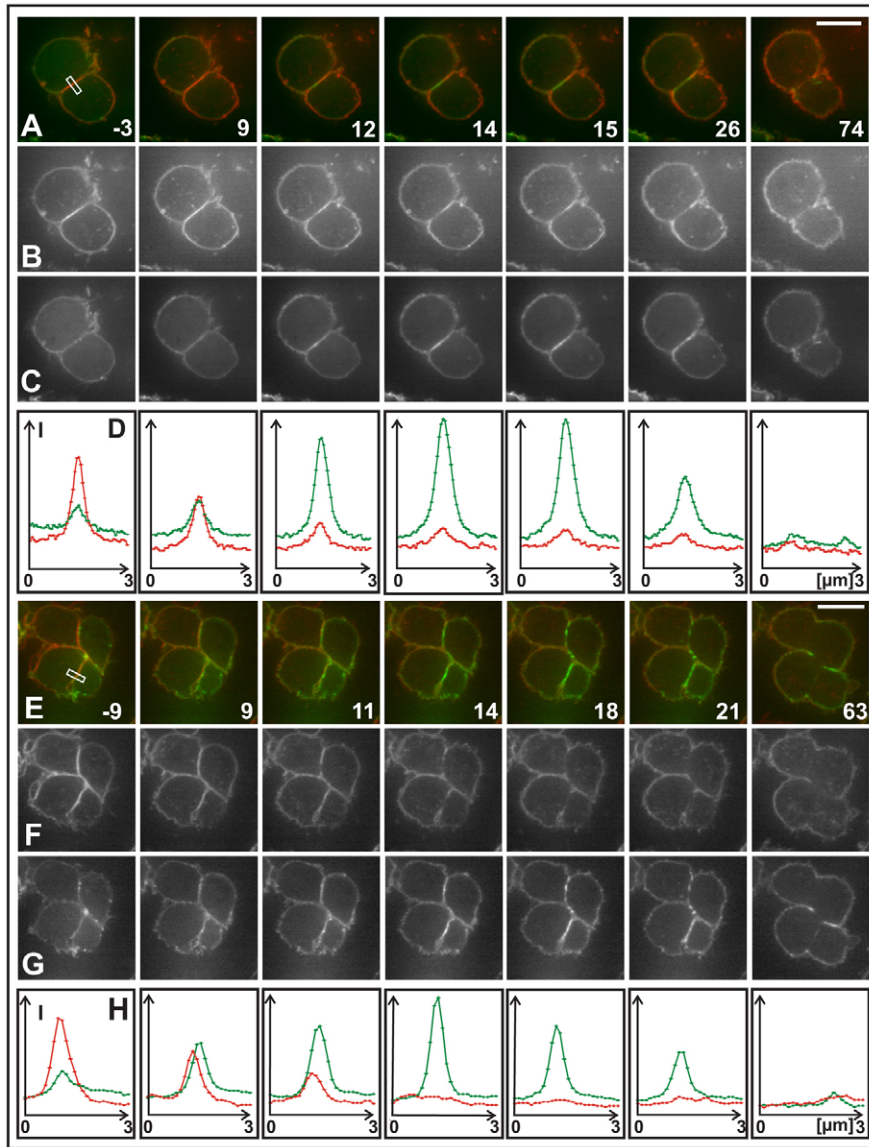


Fig. 6. Reorganization of actin during cell fusion. Cells expressing LimE Δ -GFP as a label for filamentous actin (green) were incubated with the membrane-integrating fluorescent dye FM4-64 (red) before electrofusion. (A–D) Pair of fusing cells. (E–H) Tetrad of cells fusing into one. From top to bottom, panels show merged actin and membrane labels (A,E), the membrane (B,F) and actin label (C,G) separately. (D,H) Quantification of the two labels along line scans that cross the plane of fusion. Positions of these scans are shown in A and E, respectively. Time is indicated in seconds before and after the end of electric pulsing. Scale bars: 10 μ m.

and to pull on the microtubules of *Dictyostelium* cells (Koonce et al., 1999). Accordingly, an isolated piece of the membrane will be drawn towards the centrosome of one of the fusing cells.

Persistence of microtubules during fusion

Microtubules in *Dictyostelium* cells are distinguished from mammalian ones by their extraordinary resistance to Ca^{2+} (White and Katz, 1987). They are also resistant to any ionic changes in the cytoplasm that may be caused by the electric pulses. Fig. 7A shows microtubules that penetrate the fusion zone soon after the cells are connected. In giant cells formed at the end of fusion, microtubule complexes emanate from each centrosome (supplementary material Movie 6). These microtubules may become extremely long (Fig. 7B) and often cross each other (Fig. 7C).

Discussion

Interpretation of delay times in the formation of fusion pores

In this study we explore alterations in membrane organization and actin assembly during the electrically induced fusion of intact

cells. In comparison to the fusion of lipid vesicles, the fusion of cells proceeded slowly, in the range of seconds, suggesting that retarding processes counteract the progression of membrane fusion in the compound system of lipid bilayer membrane and underlying actin network. Our data point to a local response in the actin system that results in the accumulation of filamentous actin at the sites of fusion pore formation.

According to the crystal structure of GFP, the molecule is a short cylinder of about 4.2 nm in length and 2.4 nm in diameter (Ormö et al., 1996; Yang et al., 1996). Therefore, the beginning of GFP diffusion between fusing cells indicates that pores in the contiguous membranes have reached a size of 2 to 3 nm diameter. The mixing of cells that express GFP in the cytoplasm with non-expressing cells enabled us to measure spatial profiles and flow rates of the fluorescent protein during opening of the fusion pores.

From electric pulsing to the beginning of GFP diffusion into the acceptor cell there was a delay, which varied in our experiments from less than 1 second up to 25 seconds. One reason of this variation is certainly the irregular position and

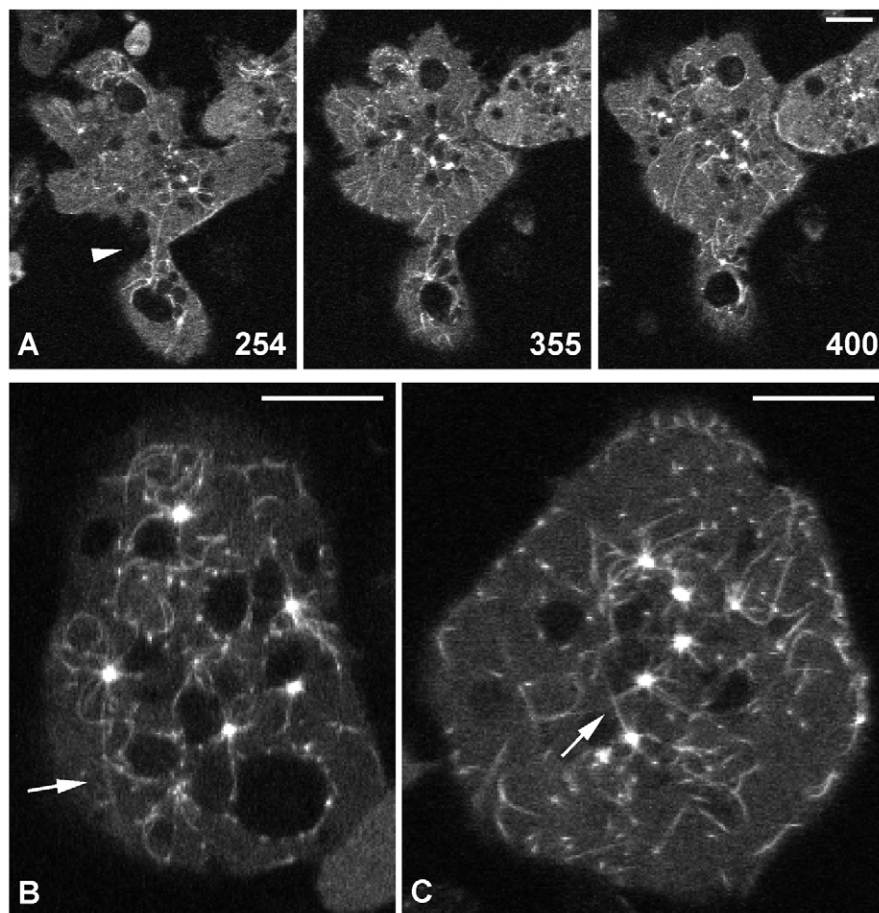


Fig. 7. Persistence of microtubules during cell fusion. The cells express GFP- α -tubulin to visualize microtubules and the centrosomes from which they emanate. (A) Three fusion stages. The arrowhead points to microtubules that cross the bridge between fusing cells. Numbers indicate seconds after the end of pulsing. The entire sequence is shown in supplementary material Movie 6. (B,C) Large cells at the end of fusion containing multiple centrosomes with associated microtubule complexes. The arrow in B points to a long microtubule, that in C to microtubules that cross each other. Scale bars: 10 μ m.

orientation of fusing cells relative to the inhomogeneous electric field. Of interest are the long delays. They indicate that the electric pulses induce a propensity for fusion that can persist for tens of seconds before pores are formed of a size that allows GFP to pass. Assuming a pathway from hydrophobic contact through a stalk state and hemifusion diaphragm to the formation of fusion pores, it is the period from the stalk to a hemifusion diaphragm in which the membrane is proposed to exist in a metastable state that does not allow the passage of aqueous solutes (Kozlovsky et al., 2004; Smirnova et al., 2010). However, for energetic reasons cells may, by the tilting of lipids, directly pass from the stalk to a modified stalk and further, by expansion of a prepore, to a fusion pore (Kuzmin et al., 2001). Moreover, earlier studies on mammalian erythrocyte ghosts (Sowers, 1986) and CHO cells (Teissié and Ramos, 1998) have indicated that cells acquire a fusogenic state that can last for minutes before they are brought into contact, this means before hemifusion of apposed membranes has an opportunity to commence (Dimitrov and Sowers, 1990). In supplementary material Movie 5, the right pair of cells appears to lack contact for 18 seconds after electric pulsing before fusion commences. Therefore, cells may arrest either in a fusogenic state that is induced in a single bilayer membrane before close cell-to-cell contacts are formed, or may arrest after stalk formation in the state of a hemifusion diaphragm that prevents GFP from exchanging between the fusing cells. Eventually, vesiculation of the membranes opens pores much

larger than required for GFP to pass (see Fig. 6; supplementary material Movie 2).

Membrane bending in cell fusion

The plasma membranes in the fusion zone are strongly bent and interdigitated (Fig. 5B–D). The close contact of membranes in this ‘fusion tangle’ will keep the cells together after cessation of the electric pulses, providing a high probability for stalk formation and hemifusion. Moreover, in these tangles the membranes are forced to assume alternately positive and negative curvatures. It is conceivable that bending of the membranes in different directions is accompanied by the redistribution of lipids and/or proteins (Roux et al., 2005; McMahon and Gallop, 2005; Lai et al., 2011), as a way of lowering the energies of the intermediate states of membrane fusion (Yang, et al., 2003).

The fusion efficiency of lipid vesicles depends on their size. Positive membrane curvature appears to be an optimal condition for fusion and progression to pore formation (Kozlov et al., 2010; Malinin et al., 2002). t-SNARE mediated fusion of giant vesicles is assisted by proteins that locally increase membrane curvature (Hui et al., 2009). Smaller vesicles with a radius of 13 nm show an enhanced formation of fusion pores relative to larger ones with a radius of 60 nm (Malinin et al., 2002). In the fusion tangles of *Dictyostelium* cells, the radii for positive membrane curvature varied between 13 and 105 nm. The smaller ones were within the

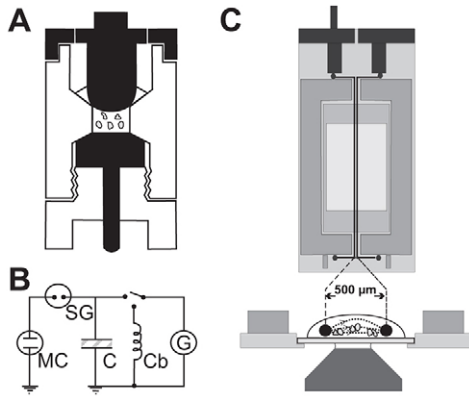


Fig. 8. Chambers used for cell fusion. (A) Chamber for mass fusion of cells, used to generate the giant cells shown in Fig. 1 and Fig. 5. The suspended cells are between two stainless steel electrodes. (B) High-voltage discharge circuit used for cell fusion. MC, measuring chamber with cell suspension; C, discharge capacitor; G, voltage generator; Cb, cable; SG, spark gap to switch the high voltage stored in the cable. (C) Microchamber for recording fluorescent protein transfer and actin reorganization upon cell fusion. For imaging cells, using a 100×1.4 NA oil Apochromate objective, the bottom of the chamber was made of a glass coverslip. Cells were fused during settling onto the glass surface. Between two electrodes of platinum-iridium wire, the cells were exposed to an inhomogeneous electric field. The field lines are dotted. Three rectangular pulses of 100 V and 0.1 seconds duration were applied in a train with intervals of 0.1 seconds, and the end of the last pulse was taken as zero time. The nominal strength of the field varied from $E_{\text{nom}}=4.5$ kV/cm close to the electrodes to $E_{\text{nom}}=3.3$ kV/cm in the middle between them.

range of sizes at which membrane curvature raises the propensity of lipid vesicles to fuse (Kozlov et al., 2010; McMahon et al., 2010), suggesting that critical steps in membrane fusion proceeded at multiple sites distributed over the entire entangled membranes.

Role of actin reorganization

The complexes of interdigitated, highly bent membranes observed in electron microscopic sections through fusing cells surrounded particle-free zones of the cytoplasm, which are typical of the cortical actin network (Fig. 5C,D). These data are in accord with those obtained by fluorescence microscopy. In cells double-labeled for the lipid membranes and filamentous actin, the membranes were seen to vesiculate in the fusion zone and the gaps between the vesicles to be bridged by networks of actin (Fig. 6A,E). In fact, filamentous actin does increase in these gaps relative to its presence in the zone of cell-to-cell contact before electric pulsing (Fig. 6D,H; supplementary material Movies 3, 4). Networks of actin filaments reduce the diffusion coefficient of GFP in cells of *D. discoideum* from $D=42 \mu\text{m}^2/\text{second}$ in the absence of filamentous actin to $D=24 \mu\text{m}^2/\text{second}$ in its presence (Potma et al., 2001). Therefore, the filling of membrane pores with filamentous actin will hinder free diffusion as long as the layer of vesiculated membranes and actin is not completely disrupted (Fig. 6; supplementary material Movies 3, 4). The assembly of actin at the gaps of fusing membranes appears to be related to the Arp2/3-associated polymerization of actin filaments at the edge of wounds cut into sea urchin coelomocytes (Henson et al., 2002) or various vertebrate cells (Vinzencz et al., 2012).

A signal that elicits actin accumulation at the vesiculating plasma membrane might be the strong curvature of the vesicle surface as judged from electron micrographs (Fig. 5B–D). Studies on the phagocytosis of particles with complex surface geometry have provided evidence for the recognition of bent regions of the plasma membrane by an I-BAR protein and local induction of actin polymerization at those regions (Clarke, et al., 2010).

Mechanically, the actin network appears to prevent the sudden rupture of the membranes that separate the fusing cells, which is observed when actin is depolymerized (see supplementary material Movie 5). This rupture contrasts to the gradual opening of fusion pores in the presence of an intact actin system, as revealed by a delay of 5 seconds between the onset of GFP flow and its maximal rate within the pair of donor and acceptor cells shown in Fig. 2. The fast progression of fusion upon the depolymerization of actin brings the rate of cell fusion closer to the rate of giant lipid vesicles in which fusion pores, once induced, expand with a velocity of 5 cm/second (Haluska et al., 2006). These data underscore the notion that in fusing cells, as compared to lipid vesicles, the actin cytoskeleton undergoing reorganization in response to electric pulsing, modulates the fusion of the plasma membranes.

In conclusion, the fusion of eukaryotic cells in response to electric pulses is complicated, relative to the fusion of lipid vesicles, by the membrane-anchored actin network. In the fusion zone, the apposed plasma membranes form tangles of highly positive and negative curvature, embedded into a network of actin filaments. This is due to the induction of actin polymerization at the sites of fusion, causing actin clusters to fill the holes within the fusing membranes. In the compound membranes of living cells, fusion is prevented for a variable number of seconds before pores are formed of about 3 nm diameter that allow GFP to pass. Eventually, the membranes vesiculate and the actin coat bridging the gaps disassembles.

Materials and Methods

Mass fusion of cells

Cells of *Dictyostelium discoideum* strain AX2-214 were cultivated in nutrient medium, washed in 17 mM K/Na-phosphate buffer, pH 6.0, and suspended in the buffer at a density of 1×10^7 cells/ml. To enhance cell contact, the cells were allowed to agglutinate under gentle shaking in a roller tube.

The experimental setup for mass fusion has been described (Neumann et al., 1980). After transfer into a chamber of 0.35 ml (Fig. 8A,B), the cells were exposed to impulses of the initial intensity $E_0=5$ kV/cm, decaying exponentially with time t according to $E(t)=E_0\exp(-t/RC)$. The sample resistance $R=2\times 10^3 \Omega$ and the discharge capacitance $C=21$ nF yielded a field decay time constant of $RC=42 \mu\text{seconds}$ for each pulse. Our standard procedure consisted of three pulses at intervals of 3 seconds.

Electron microscopy

For scanning electron microscopy, fused cells of strain AX2 that migrated on a glass coverslip were fixed for 15–45 minutes on ice with a mixture of 1% glutaraldehyde and 0.02% OsO_4 in 17 mM K/Na phosphate buffer, pH 6 or 7. After washing four times in the buffer, the cells were dehydrated in an acetone gradient, critical-point dried, and coated with 20-nm gold.

For transmission EM of sections, 2.5 minutes after electric pulsing 300 μl of the cell suspension were added to 5 ml of fixative I on ice containing 1.5% glutaraldehyde and 0.03% OsO_4 in 17 mM phosphate buffer, pH 6.0, mixed together immediately before use and kept in the dark. After 15 to 60 minutes, fixative I was replaced by fixative II, 2% glutaraldehyde, for 1 to 2 hours. After washing in phosphate buffer, cells were post-fixed with 1% OsO_4 and embedded into agar. Dehydration with ethanol for embedding in Epon included block staining with 2% uranyl acetate at the 70% ethanol step. Thin sections (50 to 70 nm) were mounted on formvar-coated grids and stained with uranyl acetate and lead citrate.

Imaging of individual fusion events in a microchamber

Cell fusion was recorded in real time by fluorescence microscopy using a Perkin-Elmer Ultra View spinning disc confocal microscope (Waltham, MA, USA). For visualizing GFP flow through fusion pores, AX2-derived cells expressing either free GFP or mRFP-LimEΔ, a label for filamentous actin (Bretschnider et al., 2004), were mixed. For studying actin reorganization during fusion, cells expressing LimEΔ-GFP were used. For membrane labeling, the styryl dye FM4-64 purchased from Invitrogen (Life Technologies Ltd, Carlsbad, California) was added (Heuser et al., 1993). Microtubules were labeled in cells expressing GFP- α -tubulin (Neujahr et al., 1998).

Cells were transferred onto a glass coverslip that served as the bottom of a microchamber (Krüss Optronic, Hamburg, Germany), modified to permit proper positioning of the cells between two electrode wires of 200 μ m diameter. The center-to-center distance of the wires was 500 μ m (Fig. 8C). Trains of three electric pulses were generated by a Biojet CF 50 (Krüss Optronic).

To determine diffusion of free GFP in the cytoplasm, fluorescence intensities were corrected for background in the extracellular space and for photobleaching. In each image series, a square free of cells was used to determine background, and the average of all frames in the series was subtracted from the fluorescence intensities within cells. The frames recorded before electric pulsing were used to determine the bleaching rate. In 14 cells from four recordings an average decay of $y=e^{0.0018x}$ (x , frame number) for an average frame-to-frame interval of 480 milliseconds was determined and used to eliminate the contribution of bleaching from the data.

Volumes of fusing cells were determined at the end of fusion from z-stacks of confocal sections recorded at a step size of 0.2 μ m from bottom to top of the cells, using remnants of actin and the constriction between cells recorded at earlier fusion stages for positioning of the cell-cell boundary.

Simulation of diffusion in fusing cells

For the simulations we used Smoldyn Version 2.28 (Andrews et al., 2010), which is freely available at www.smoldyn.org. As diffusion coefficient for GFP in the lumen of the cells we chose $D=25 \mu\text{m}^2/\text{second}$. For each of the four simulations shown in Fig. 4B–D we ran 25 samples, each with 10,000 particles. In all simulations, pore expansion occurred in time steps of 1 milliseconds over a total of 10 seconds up to a final radius $r=3.4 \mu\text{m}$. This size is sufficient as the flux decreases in the simulations already before the maximum pore size is reached. The Smoldyn configuration files for our simulations are available upon request from the corresponding author.

Acknowledgements

We thank Dr. C.-R. Rabl, University of Bielefeld, for the design of a modified microchamber and Richard Guggenheim, University of Basel, for the scanning electron micrographs. The transmission EM work was performed by Michael Claviez.

Author contributions

G.G. planned experiments and evaluated the results, M.E. performed experiments and analyzed data, J.P. and R.N. performed fusion experiments, U.S. and M.H. computed the simulations and E.N. designed equipment and analyzed data.

Funding

The work of G.G. was supported by the Max Planck Society and that of M.H. by the German Federal Ministry of Education and Research (BMBF) program MechanoSys [grant number 0315501C to M.H.].

Supplementary material available online at

<http://jcs.biologists.org/lookup/suppl/doi:10.1242/jcs.124073/-/DC1>

References

Andrews, S. S., Addy, N. J., Brent, R. and Arkin, A. P. (2010). Detailed simulations of cell biology with Smoldyn 2.1. *PLOS Comput. Biol.* **6**, e1000705.

Blangero, C., Rols, M. P. and Teissie, J. (1989). Cytoskeletal reorganization during electric-field-induced fusion of Chinese hamster ovary cells grown in monolayers. *Biochim. Biophys. Acta* **981**, 295–302.

Boettcher, B., Marquez-Lago, T. T., Bayer, M., Weiss, E. L. and Barral, Y. (2012). Nuclear envelope morphology constrains diffusion and promotes asymmetric protein segregation in closed mitosis. *J. Cell Biol.* **197**, 921–937.

Bretschnider, T., Diez, S., Anderson, K., Heuser, J., Clarke, M., Müller-Taubenberger, A., Köhler, J. and Gerisch, G. (2004). Dynamic actin patterns and Arp2/3 assembly at the substrate-attached surface of motile cells. *Curr. Biol.* **14**, 1–10.

Chernomordik, L. V. and Kozlov, M. M. (2008). Mechanics of membrane fusion. *Nat. Struct. Mol. Biol.* **15**, 675–683.

Clarke, M., Maddera, L., Engel, U. and Gerisch, G. (2010). Retrieval of the vacuolar H-ATPase from phagosomes revealed by live cell imaging. *PLoS ONE* **5**, e8585.

Dimitrov, D. S. and Sowers, A. E. (1990). A delay in membrane fusion: lag times observed by fluorescence microscopy of individual fusion events induced by an electric field pulse. *Biochemistry* **29**, 8337–8344.

Gerisch, G., Bretschnider, T., Müller-Taubenberger, A., Simmeth, E., Ecke, M., Diez, S. and Anderson, K. (2004). Mobile actin clusters and traveling waves in cells recovering from actin depolymerization. *Biophys. J.* **87**, 3493–3503.

Haluska, C. K., Riske, K. A., Marchi-Artzner, V., Lehn, J. M., Lipowsky, R. and Dimova, R. (2006). Time scales of membrane fusion revealed by direct imaging of vesicle fusion with high temporal resolution. *Proc. Natl. Acad. Sci. USA* **103**, 15841–15846.

Henson, J. H., Nazarian, R., Schulberg, K. L., Trabosh, V. A., Kolnik, S. E., Burns, A. R. and McPartland, K. J. (2002). Wound closure in the lamellipodia of single cells: mediation by actin polymerization in the absence of an actomyosin purse string. *Mol. Biol. Cell* **13**, 1001–1014.

Heuser, J., Zhu, Q. and Clarke, M. (1993). Proton pumps populate the contractile vacuoles of Dictyostelium amoebae. *J. Cell Biol.* **121**, 1311–1327.

Hui, E., Johnson, C. P., Yao, J., Dunning, F. M. and Chapman, E. R. (2009). Synaptotagmin-mediated bending of the target membrane is a critical step in Ca(2+)-regulated fusion. *Cell* **138**, 709–721.

Khan, S., Reese, T. S., Rajpoot, N. and Shabbir, A. (2012). Spatiotemporal maps of CaMKII in dendritic spines. *J. Comput. Neurosci.* **33**, 123–139.

Kiessling, V., Domanska, M. K. and Tamm, L. K. (2010). Single SNARE-mediated vesicle fusion observed in vitro by polarized TIRFM. *Biophys. J.* **99**, 4047–4055.

Kjaergaard, J., Shimizu, K. and Shu, S. (2003). Electrofusion of syngeneic dendritic cells and tumor generates potent therapeutic vaccine. *Cell. Immunol.* **225**, 65–74.

Koonce, M. P., Köhler, J., Neujahr, R., Schwartz, J.-M., Tikhonenko, I. and Gerisch, G. (1999). Dynein motor regulation stabilizes interphase microtubule arrays and determines centrosome position. *EMBO J.* **18**, 6786–6792.

Kozlov, M. M., McMahon, H. T. and Chernomordik, L. V. (2010). Protein-driven membrane stresses in fusion and fission. *Trends Biochem. Sci.* **35**, 699–706.

Kozlovsky, Y., Efrat, A., Siegel, D. A. and Kozlov, M. M. (2004). Stalk phase formation: effects of dehydration and saddle splay modulus. *Biophys. J.* **87**, 2508–2521.

Kuzmin, P. I., Zimmerberg, J., Chizmadzhev, Y. A. and Cohen, F. S. (2001). A quantitative model for membrane fusion based on low-energy intermediates. *Proc. Natl. Acad. Sci. USA* **98**, 7235–7240.

Lai, A. L., Tamm, L. K., Ellena, J. F. and Cafiso, D. S. (2011). Synaptotagmin 1 modulates lipid acyl chain order in lipid bilayers by demixing phosphatidylserine. *J. Biol. Chem.* **286**, 25291–25300.

Lo, M. M. S., Tsong, T. Y., Conrad, M. K., Strittmatter, S. M., Hester, L. D. and Snyder, S. H. (1984). Monoclonal antibody production by receptor-mediated electrically induced cell fusion. *Nature* **310**, 792–794.

Malinin, V. S., Frederik, P. and Lentz, B. R. (2002). Osmotic and curvature stress affect PEG-induced fusion of lipid vesicles but not mixing of their lipids. *Biophys. J.* **82**, 2090–2100.

Markin, V. S. and Albanesi, J. P. (2002). Membrane fusion: stalk model revisited. *Biophys. J.* **82**, 693–712.

Markin, V. S., Kozlov, M. M. and Borovjagin, V. L. (1984). On the theory of membrane fusion. The stalk mechanism. *Gen. Physiol. Biophys.* **5**, 361–377.

McMahon, H. T. and Gallop, J. L. (2005). Membrane curvature and mechanisms of dynamic cell membrane remodeling. *Nature* **438**, 590–596.

McMahon, H. T., Kozlov, M. M. and Martens, S. (2010). Membrane curvature in synaptic vesicle fusion and beyond. *Cell* **140**, 601–605.

Medalia, O., Weber, I., Frangakis, A. S., Nicastro, D., Gerisch, G. and Baumeister, W. (2002). Macromolecular architecture in eukaryotic cells visualized by cryoelectron tomography. *Science* **298**, 1209–1213.

Neujahr, R., Albrecht, R., Köhler, J., Matzner, M., Schwartz, J.-M., Westphal, M. and Gerisch, G. (1998). Microtubule-mediated centrosome motility and the positioning of cleavage furrows in multinucleate myosin II-null cells. *J. Cell Biol.* **111**, 1227–1240.

Neumann, E., Gerisch, G. and Opatz, K. (1980). Cell fusion induced by high electric impulses applied to Dictyostelium. *Naturwissenschaften* **67**, 414–415.

Neumann, E., Sowers, A. E. and Jordan, C. A. (eds) (1989). *Electroporation and Electrofusion in Cell Biology*. New York, NY: Plenum Press.

Ormö, M., Cubitt, A. B., Kallio, K., Gross, L. A., Tsien, R. Y. and Remington, S. J. (1996). Crystal structure of the Aequorea victoria green fluorescent protein. *Science* **273**, 1392–1395.

Potma, E. O., de Boeij, W. P., Bosgraaf, L., Roelofs, J., van Haastert, P. J. and Wiersma, D. A. (2001). Reduced protein diffusion rate by cytoskeleton in vegetative and polarized Dictyostelium cells. *Biophys. J.* **81**, 2010–2019.

Qian, S. and Huang, H. W. (2012). A novel phase of compressed bilayers that models the prestalk transition state of membrane fusion. *Biophys. J.* **102**, 48–55.

Roux, A., Cuvelier, D., Nassoy, P., Prost, J., Bassereau, P. and Goud, B. (2005). Role of curvature and phase transition in lipid sorting and fission of membrane tubules. *EMBO J.* **24**, 1537–1545.

Senda, M., Takeda, J., Abe, S. and Nakamura, T. (1979). Induction of cell fusion of plant protoplasts by electrical stimulation. *Plant Cell Physiol.* **20**, 1441–1443.

Shillock, J. C. and Lipowsky, R. (2005). Tension-induced fusion of bilayer membranes and vesicles. *Nat. Mater.* **4**, 225–228.

- Smirnova, Y. G., Marrink, S. J., Lipowsky, R. and Knecht, V.** (2010). Solvent-exposed tails as prestalk transition states for membrane fusion at low hydration. *J. Am. Chem. Soc.* **132**, 6710-6718.
- Sowers, A. E.** (1986). A long-lived fusogenic state is induced in erythrocyte ghosts by electric pulses. *J. Cell Biol.* **102**, 1358-1362.
- Teissié, J. and Rols, M. P.** (1994). Manipulation of cell cytoskeleton affects the lifetime of cell membrane electroporation. *Ann. New York Acad. Sci.* **720**, 98-110.
- Teissié, J. and Ramos, C.** (1998). Correlation between electric field pulse induced long-lived permeabilization and fusogenicity in cell membranes. *Biophys. J.* **74**, 1889-1898.
- Vinzenz, M., Nemethova, M., Schur, F., Mueller, J., Narita, A., Urban, E., Winkler, C., Schmeiser, C., Koestler, S. A., Rottner, K. et al.** (2012). Actin branching in the initiation and maintenance of lamellipodia. *J. Cell Sci.* **125**, 2775-2785.
- White, E. and Katz, E. R.** (1987). Biochemical and genetic approaches to microtubule function in *Dictyostelium discoideum*. In: *Methods in Cell Biology*, Vol. 28: *Dictyostelium discoideum – Molecular Approaches to Cell Biology* (ed. James A. Spudich).
- Yang, L. and Huang, H. W.** (2002). Observation of a membrane fusion intermediate structure. *Science* **297**, 1877-1879.
- Yang, F., Moss, L. G. and Phillips, G. N., Jr** (1996). The molecular structure of green fluorescent protein. *Nat. Biotechnol.* **14**, 1246-1251.
- Yang, L., Ding, L. and Huang, H. W.** (2003). New phases of phospholipids and implications to the membrane fusion problem. *Biochemistry* **42**, 6631-6635.
- Zimmermann, U. and Vienken, J.** (1982). Electric field-induced cell-to-cell fusion. *J. Membr. Biol.* **67**, 165-182.